ALMA Memo No. 517
Turbulence simulations of dry and wet phase fluctuations at Chajnantor.
Part I: The daytime convective boundary layer.

Alison Stirling[1], John Richer[1], Richard Hills[1], Adrian Lock[2]
1 University of Cambridge, 2 Met Office, UK

April 18, 2005

1 Abstract

We have performed numerical simulations of the atmosphere for typical daytime convective conditions at Chajnantor, and derived the resulting wet and dry contributions to the atmospheric phase fluctuations. The simulations show that:
◦ Dry phase fluctuations are concentrated in two layers – near to the ground, and at the temperature inversion. The wet fluctuations are concentrated at the inversion, while the total phase fluctuations are more uniformly distributed within the convective layer. This is because of significant positive and negative correlations between the dry and wet refractive index fluctuations.
◦ The phase structure function is well described by a Kolmogorov turbulence spectrum on small scales, with a turn over on a scale of order the depth of the boundary layer.
◦ The variation of total r.m.s. phase with elevation shows a dependence on the square root of air mass for the total phase, but the dry component shows a linear variation with air mass, and the wet component varies as air mass to the power 0.75.

A scaling analysis has been used to relate the r.m.s. wet and dry phase fluctuations to the vertical profiles of temperature and water vapour so that an estimate of the phase fluctuations at Chajnantor can be obtained from radiosonde data.
◦ Using this approach, the r.m.s. dry fluctuations along a single line of sight are found to be 100–200 μm at the 25–75 percentiles respectively, and the equivalent wet fluctuations are found to lie in the range 180–530 μm. The total r.m.s. path fluctuations were estimated to be 240–525 μm, and we have compared these estimates with independent measurements of the total r.m.s. phase obtained from interferometric measurements (Evans *et al.*, 2003), and these show excellent agreement.
◦ The correlation coefficient between total and wet phase fluctuations is estimated, and this is found to lie in the range 0.75–0.97 at the 25–75 percentiles. This suggests that, even under conditions where the dry phase fluctuations are expected to be at their highest, water vapour radiometry is expected to be able to remove a high percentage of phase fluctuations at Chajnantor.

2 Introduction

Atmospheric phase calibration is expected to play a significant role in determining the performance of ALMA. The phase calibration procedure will use a combination of fast switching to a reference point source, and continuous on-source water vapour radiometry. Since fast switching is sensitive to the total atmospheric phase variation, while water vapour radiometry only to the wet component of phase, the performance of any phase correction strategy is likely to depend on the relative contributions to the wet and dry phase variations. It is therefore important to be able to quantify the expected wet and dry contributions to phase variation at the ALMA site in Chajnantor.

While there have been measurements of the total phase variation from an interferometer operating on a 300 m baseline (*e.g.* Butler, 2001; memo 365), there has so far been little work on measuring the relative amplitudes of the dry and wet contributions to phase fluctuations. In this report, we address the issue of phase fluctuations during the daytime – these are expected to be generated largely by convective activity which is driven by the solar heating of the ground. We shall address in a second memo (518) the typical night time conditions, where turbulence is driven by wind shear, and the atmosphere is very stable.

Convection causes air to mix vertically, and so in the presence of vertical gradients in temperature and water vapour, it can lead to significant refractive index fluctuations. Of particular interest is the dynamics around temperature inversions, which are a common feature during the daytime at Chajnantor, as these are likely to be a dominant source of dry and wet phase fluctuations. Convection in the boundary layer (corresponding in general to the lowest few hundred metres of the atmosphere) has been studied extensively in meteorology, with field campaigns, numerical models and theoretical work that has focused on understanding how convection affects the statistics of various atmospheric parameters, for example the variance and vertical fluxes of temperature and water vapour.

In this report we present simulations of convection that resemble the daytime conditions at Chajnantor. From these simulations we have been able to measure the relative contributions to the dry and wet phase fluctuations as well as the phase structure function. We have combined results from the simulations with theoretical scaling relations to produce a relationship between the variance in atmospheric phase and the vertical profiles of water vapour and temperature. With such a relationship, we can then calculate the expected dry and wet contributions to the fluctuations directly from radiosonde profiles taken from the site (Radford *et al.*, 2000).

The layout of this report is as follows: Section 3 provides an outline of the relationship between refractive index and temperature and water vapour variations. In Section 4 we describe the turbulence simulations of the daytime atmosphere at Chajnantor, and present some typical results from the simulations – including vertical profiles of r.m.s. temperature and water vapour fluctuations, and the phase structure function. In Section 5 we give a summary of the theoretical scaling relations that have been found to apply to convection in the boundary layer, and compare the performance of these relations against the results from the numerical turbulence code. In Section 6 we show how the predictions for the variance in temperature and water vapour fluctuations can be used to give an estimate for the expected dry and wet path-length fluctuations. In Section 7 we apply our analysis to some radiosonde data from Chajnantor, obtaining estimates for the dry and wet components of atmospheric phase. The conclusions are summarised in Section 8, and the appendix in Section 10 provides an outline of a few basic concepts and

definitions that are used throughout this report.

3 Refractive index fluctuations

In this section we show how refractive index fluctuations are related to fluctuations in water vapour and potential temperature, θ, (where potential temperature is a measure of temperature corrected to a standard reference pressure) [1]. The refractive index of the atmosphere at 100 GHz is given by the Smith-Weintraub equation:

$$n - 1 = 10^{-6}\Big[\alpha\frac{P_d}{T} + \beta\frac{P_w}{T} + \gamma\frac{P_w}{T^2}\Big], \tag{1}$$

where P_d, P_w are the partial pressures for dry air and water vapour respectively, and $\alpha = 77.6 \times 10^{-2}$ K Pa^{-1}, $\beta = 64.8 \times 10^{-2}$ K Pa^{-1}, and $\gamma = 3.776 \times 10^{3}$ K^2 Pa^{-1}. This equation can be written in terms of the total air density, ρ_T by using the ideal gas equation for the dry air and water vapour components respectively:

$$P_d = \rho_d RT/\mathcal{M}_d, \qquad P_w = \rho_w RT/\mathcal{M}_w \tag{2}$$

where ρ_d is the density of the dry air, and ρ_w is the density of the water vapour, $R = 8.314$ J mol^{-1} K^{-1} is the universal gas constant, $\mathcal{M}_d = 28.96$ g mol^{-1} is the molecular weight of dry air in the troposphere, and $\mathcal{M}_v = 18.02$ g mol^{-1} is the equivalent for water vapour. The total pressure is given by the sum of the partial pressures, and the total density is given by the sum of the component densities. Substituting into equation 1, and setting $\rho_w = q\rho_T$, where q is the mass fraction of water vapour, we can write:

$$n - 1 = \alpha\frac{R\rho_T}{\mathcal{M}_d} + \left(\frac{\beta}{\mathcal{M}_v} - \frac{\alpha}{\mathcal{M}_d}\right) Rq\rho_T + \gamma\frac{Rq\rho_T}{\mathcal{M}_v T}, \tag{3}$$

where we have regrouped the first two terms to express the dry component in terms of the total density. Since the temperature is of order 300 K at its peak value, $\gamma/(T\mathcal{M}_v) >> |\beta/\mathcal{M}_v - \alpha/\mathcal{M}_d|$, and so we will neglect the second term from now on. The next stage is to consider fluctuations in refractive index about its mean value by letting $\rho_T = \overline{\rho_T} + {\rho_T}'$, $q = \overline{q} + q'$, $T = \overline{T} + T'$. Neglecting second order fluctuating terms, this gives:

$$n' = \frac{\alpha R}{\mathcal{M}_d}{\rho_T}' + \gamma\frac{R}{\mathcal{M}_v}\left\{\left(\frac{q'\rho_T + q\rho_T'}{T}\right) - \frac{T'}{T^2}q\rho_T\right\}. \tag{4}$$

Now since the dominant source of density fluctuations is from fluctuations in temperature, with pressure fluctuations contributing only at the 1% level (*e.g.* Garratt, 1992), we can rewrite $\rho_T'/\overline{\rho}_T = T'/\overline{T} = \theta'/\overline{\theta}$ so that:

$$n' = \left(\alpha\frac{R\overline{\rho}_T}{\mathcal{M}_d\overline{\theta}}\right)\theta' + \left(\gamma\frac{R}{\mathcal{M}_v}\frac{\overline{\rho}_T}{\overline{T}}\right)q'. \tag{5}$$

So the refractive index fluctuations to first order depend on fluctuations in the potential temperature, and the water vapour content. These are referred to as the dry and wet components of the refractive index respectively. In the rest of this memo we shall estimate the relative contributions of the dry and wet components using a combination of numerical simulations and theoretical scaling laws.

[1] See Section 10 for a definition of potential temperature.

4 Simulations of daytime convection at Chajnantor

4.1 Introduction

In order to analyse the structure of the atmosphere during convection, we have simulated an atmosphere that would be expected to be typical of daytime convective conditions at Chajnantor. In subsection 4.2 we describe the code used to simulate this atmosphere, and in subsection 4.3 we describe how the simulation was initiated to obtain a realistic convective atmosphere. Some output from the model is presented in subsection 4.4.

4.2 Met Office Large Eddy Model

The turbulence model used for this work is version 2.3 of the Met Office Large Eddy Model, which is documented in Gray et al (2001). This is a high resolution numerical model that can be used to simulate a wide range of turbulent-scale and cloud-scale phenomena. The model uses a technique in which the Navier-Stokes equations are filtered onto a grid, allowing turbulent motions (or eddies) larger than the size of the grid to be modelled explicitly. Turbulent motions smaller than the grid scale are parametrised by assuming that there is a Kolmogorov energy cascade from eddies on the grid scale down to smaller scales, and that energy is finally dissipated as heat on the molecular scale. The model tracks the temperature, pressure and velocity of the air as well as the water vapour content.

4.3 Model set up

The simulations used here have horizontally cyclic boundary conditions, with a rigid lid upper boundary condition at 1.4 km. The vertical grid spacing varies with height, with a spacing of 20 m in the lowest 300 m of the domain to capture the smaller turbulent eddies that are found close to the ground, and decreasing to 10 m close to the temperature inversion at 800 m, where there are steep temperature changes with height. The grid spacing then increases uniformly to 45 m at the top of the domain, where there is little motion of the atmosphere. Results focus on output from 3D simulations using a horizontal resolution of 50 m, and domain size of 4.8 km. Our choice of simulation configuration and dimension is a compromise between requiring a large enough domain to sample a statistically significant number of convective cells, and requiring high enough resolution to capture phase behaviour on scales of interest to ALMA.

The forcing applied to the model was designed to give an idealised representation of the mean daytime surface and atmospheric heating experienced at Chajnantor. Solar heating was represented as a constant surface heat flux of 200 W m^{-2}. This was estimated by assuming that 75% of the incident solar radiation reaches the ground (1370 W m^{-2} at the summer solstice), with the rest being either reflected or absorbed by the atmosphere. Of the radiation reaching the ground we assume that 60% is reflected (*i.e.* the albedo is 0.6, which is representative of soil containing no vegetation, *e.g.* Baumer, 1990), and that the surface heating varies sinusoidally so that the mean value for each day is half the maximum value. The surface heat flux can be transferred to the atmosphere from the ground in two ways – via conduction of the heat to air molecules at the surface (known as sensible heating), or via evaporation of ground-based water which is

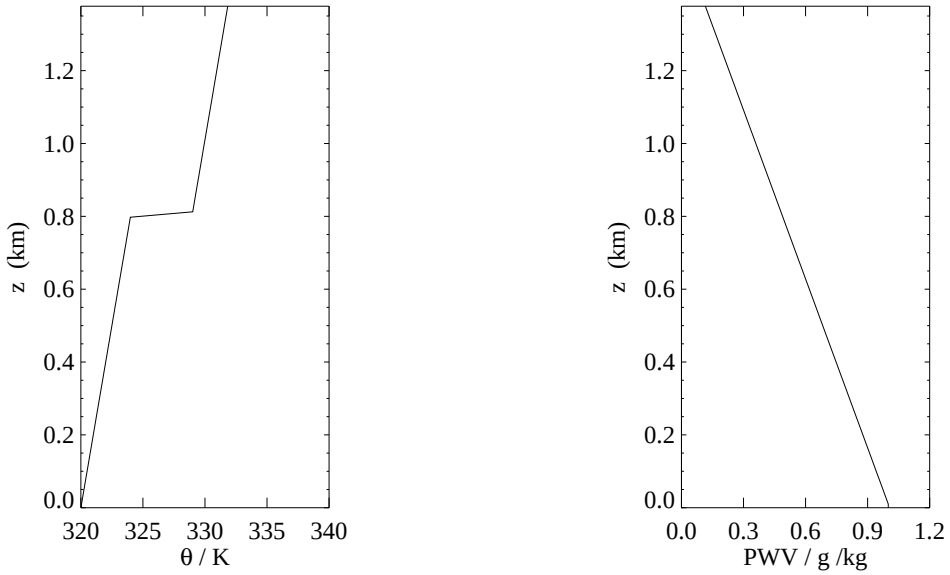

Figure 1: Initial potential temperature and moisture profiles used in the simulation.

then released into the air (known as latent heating). The dry conditions at Chajnantor suggest that the latent heating from the ground is likely to be small, but not necessarily zero. In view of the absence of this data from the site, we have considered two scenarios – one where the latent heat transfer is zero, and all the surface heat transfer is via sensible heating (simulation A); and another where the latent heat is set to $25\,\mathrm{Wm}^{-2}$, with the sensible heat being reduced accordingly to $175\,\mathrm{Wm}^{-2}$ (simulation B)(see Table 1 for a summary.)

The initial temperature and moisture profiles represent idealised conditions taken from radiosonde profiles, and are shown in Fig. 1. A mean geostrophic wind of $5\,\mathrm{m\,s}^{-1}$ was applied at the surface, increasing to $11.5\,\mathrm{m\,s}^{-1}$ at 1 km, and the Coriolis parameter, f, was set to -6×10^{-5} s^{-1} (appropriate for the latitude at Chajnantor). The surface roughness of the ground was set to 1 cm, which is typical of soils with no vegetation (*e.g.* Garratt, 1992). The simulations were run to represent a few hours of atmospheric motion, allowing time for the simulation to respond to the surface heating, and set up convective plumes in the domain.

Simulation	Surface sensible heat flux / Wm^{-2}	Surface latent heat flux / Wm^{-2}	Output Times / Hrs
A	200	0	2, 2.5, 3, 3.5, 4, 4.5
B	175	25	2, 2.5, 3, 3.5

Table 1: Summary of the simulations and output times used for the scaling analysis in Section 5.

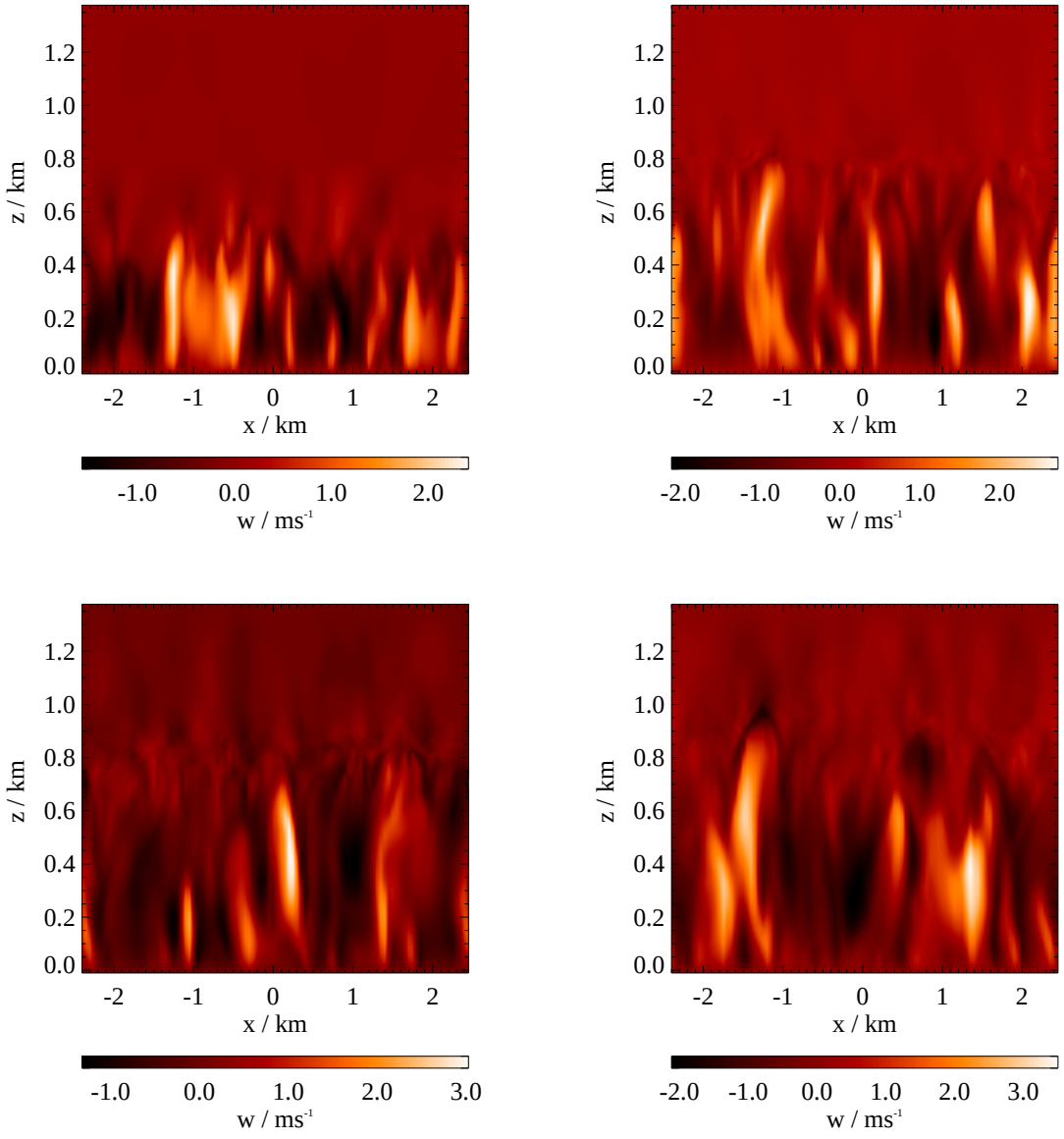

Figure 2: Contours of vertical velocity taken from simulation B through vertical slices of the domain after 0.25 hours (top left), 0.75 hours (top right), 1.5 hours (bottom left), and 2 hours (bottom right).

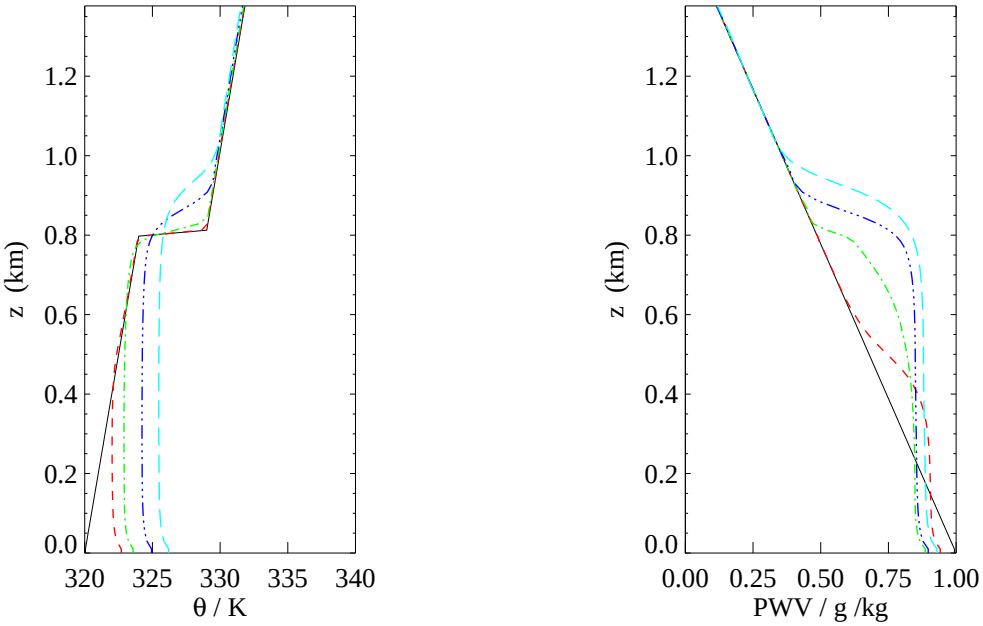

Figure 3: The evolution of mean potential temperature (left) and water vapour (right) profiles from simulation B. The different lines represent different times during the simulation: 0 hours (solid lines), 0.25 hours (dashed), 0.75 hours (dot-dashed), 1.5 hours (dot-dot-dot-dashed), and 2 hours (long dashed).

4.4 Model Output

4.4.1 Mean temperature and water vapour profiles

Convective activity was established quickly in the simulations and the atmospheric motion can be seen in Fig. 2, which shows contours of vertical velocity as the simulation progresses. Narrow plumes of rapidly ascending air are accompanied by wider regions of slowly descending air. As the simulation evolves the maximum height and velocity of the plume increases.

Figure 3 shows the mean potential temperature and water vapour profiles at different time intervals through the simulation. The effect of the convective motion is to reduce the vertical gradient in potential temperature and water vapour below the inversion, which is achieved through vertical mixing. Below 25 m the potential temperature has a negative gradient with height, which is generated by the surface heating. In this region the atmosphere is unstable, and this acts as the energy source for the convective motion.

As the day continues, the inversion is gradually eroded, with convective plumes overshooting into the inversion, and transferring air of high potential temperature above the inversion down into the region below the inversion. The erosion process increases in speed as the inversion strength (and therefore the energy barrier) is weakened. The distribution of water vapour becomes increasingly well mixed as a result of the convective motion, with the top of the well-mixed zone being set by the top of the inversion.

4.4.2 Fluctuations in temperature and water vapour

Figures 4 and 5 show the spatial fluctuations in the temperature and moisture fields across vertical and horizontal slices in the domain and after two hours of simulation. It shows that the largest fluctuations appear to be concentrated around the temperature inversion, where the gradients in temperature and moisture are steepest. This can be seen clearly in Fig. 6 which shows the r.m.s. temperature and moisture fluctuations with height. There is also a significant contribution to the temperature variance close to the ground, where the injection of heat gives rise to a significant temperature gradient. This effect is considerably smaller in the water vapour field because of the lower latent heat flux. As the simulation progresses, the height of the inversion lifts, and becomes shallower. The weakening of the inversion allows the plumes to penetrate further into the inversion, and so the layer of 'high-variance' fluctuations thickens.

We also consider the cross-correlation of temperature and water vapour fluctuations changes with height. We define a cross-correlation parameter, ξ, as follows:

$$\xi\left(z\right) = \frac{\left\langle \theta'\left(z\right) q'\left(z\right)\right\rangle}{\left\langle \theta'^{2}\left(z\right)\right\rangle^{1/2}\left\langle q'^{2}\left(z\right)\right\rangle^{1/2}} \tag{6}$$

where angle brackets indicate a spatial average in the horizontal. Figure 6 shows how this cross-correlation parameter changes with height. At low levels, the water vapour and temperature fluctuations are positively correlated, while at higher levels (just above the temperature inversion), they become anti-correlated. This can be explained by considering the convective plumes, which are the dominant source of the correlation. At low levels the plumes are positively buoyant, and they transport air from the ground upwards. The air at the ground contains more water vapour than higher up, and so the plumes have both a positive temperature difference and a positive water vapour difference compared with the surroundings. At higher levels, however, the plume loses its buoyancy when it encounters the temperature inversion, and becomes negatively buoyant. The plume still has more water vapour than the surrounding air, and so there is a tendency for the temperature and moisture fluctuations at and above the inversion to become anti-correlated.

4.4.3 Phase Structure function

Next we calculate the phase structure function for vertical lines of sight through the simulations. (We will consider how the r.m.s. path varies with elevation in Subsection 4.4.4.) The structure function is defined as:

$$\begin{aligned} S(\Delta r) &= \left\langle \left[\phi\left(r\right) - \phi\left(r+\Delta r\right)\right]^{2}\right\rangle & (7)\\ &= 2[\left\langle \phi^{2}\right\rangle - \left\langle \phi\left(r\right)\phi\left(r+\Delta r\right)\right\rangle], & (8) \end{aligned}$$

where $\phi\left(r\right)$ is the phase at position r, and $\phi\left(r+\Delta r\right)$ is the phase at a point a distance Δr away. We can measure the phase by calculating the path length, $\mathcal{L}$, (where $\mathcal{L} = \phi\lambda/2\pi$), through the simulations by integrating the refractive index, n as derived from equation 1, with respect to distance along the line sight, y, *i.e.* :

$$\mathcal{L} = \int n\left(y\right) dy, \tag{9}$$

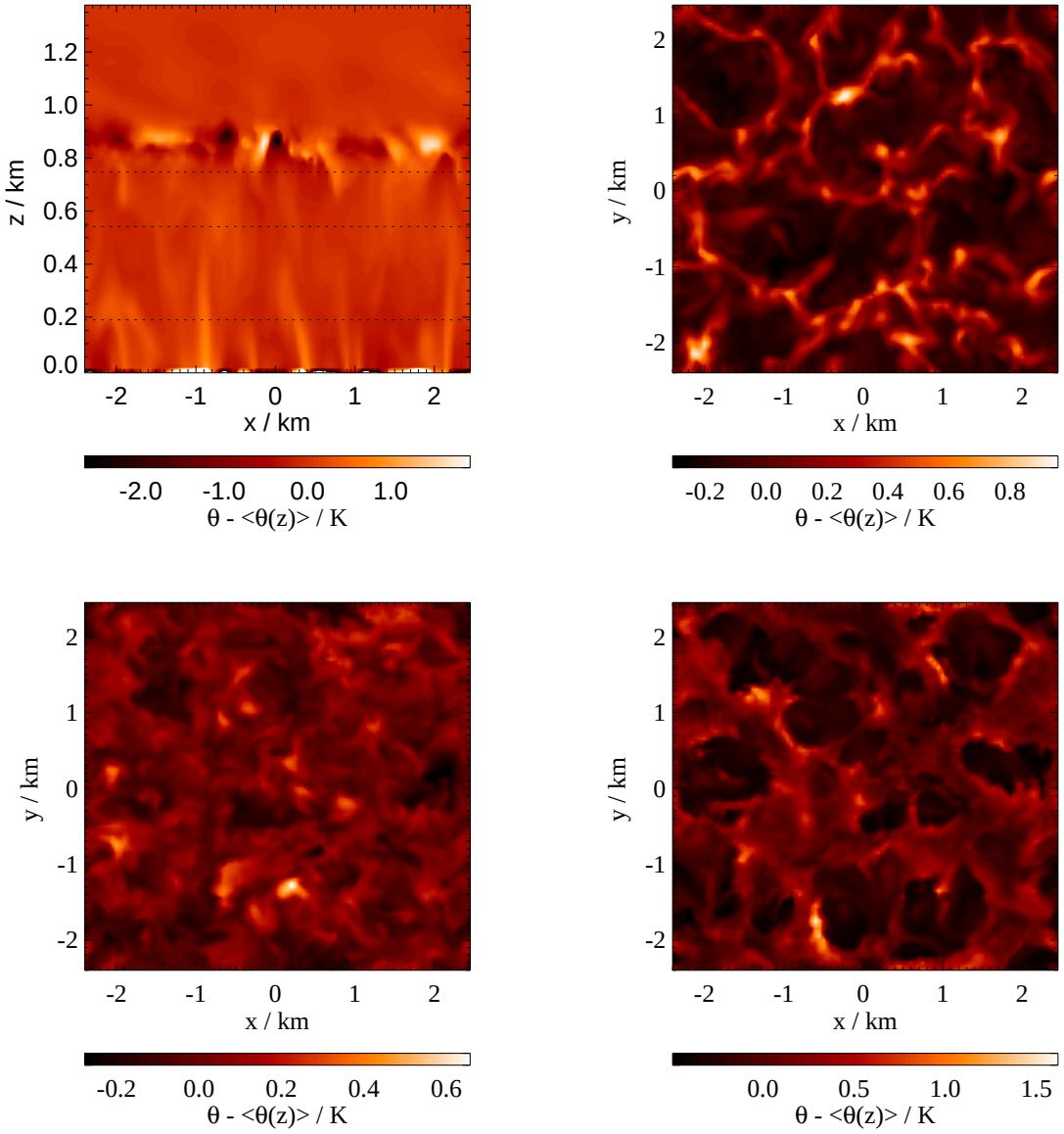

Figure 4: Contours of potential temperature fluctuations in simulation A after 2.0 hours. Fluctuations are taken about the mean value at each height through slices of the simulation domain. Top left is a vertical slice, the rest are horizontal slices taken at different heights throughout the domain indicated by the dashed lines: top right is at 200 m, bottom left is at 550 m, bottom right is at 750 m.

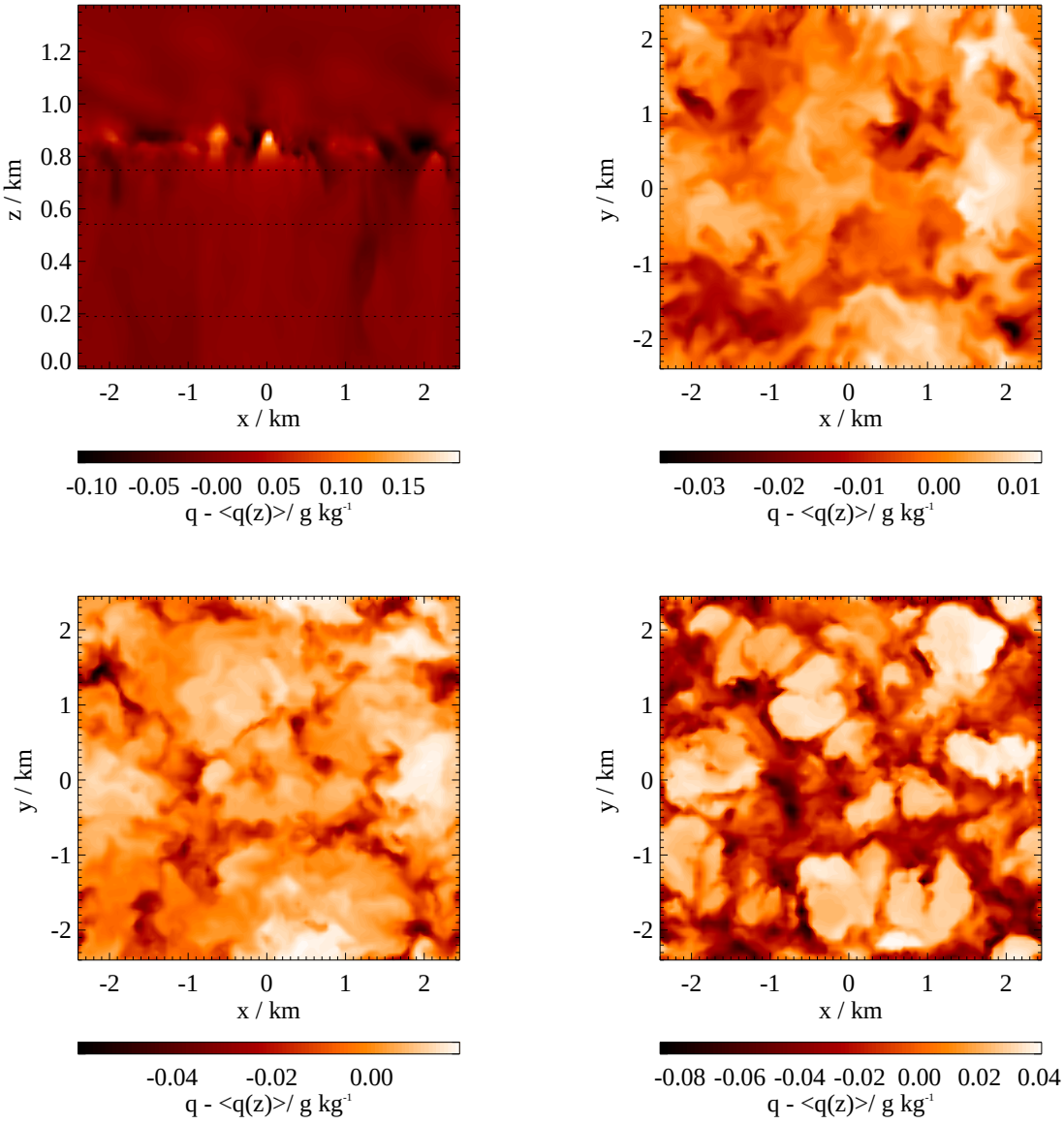

Figure 5: Contours of water vapour fluctuations in simulation A after 2.0 hours. Fluctuations are taken about the mean value at each height through slices of the simulation domain. Top left is a vertical slice, the rest are horizontal slices taken at different heights throughout the domain indicated by the dashed lines: top right is at 200 m, bottom left is at 550 m, bottom right is at 750 m.

where the units of $\mathcal{L}$, are the same as y.

We can also calculate the contributions from dry and wet phase fluctuations by separating the phase into dry and wet components, *i.e.* $\phi = \phi_d + \phi_w$, where ϕ_d is calculated using the first term in equation 1, and ϕ_w is calculated using the second and third terms in equation 1. For the structure function we then have

$$\frac{S(\Delta r)}{2} = \langle\phi_d^2\rangle - \langle\phi_d(r)\,\phi_d(r')\rangle + \langle\phi_w^2\rangle - \langle\phi_w(r)\,\phi_w(r')\rangle + 2\langle\phi_d\phi_w\rangle - 2\langle\phi_d(r)\,\phi_w(r')\rangle \quad (10)$$

$$\equiv \overbrace{\qquad S_d\,(\Delta r) \qquad}^{} + \overbrace{\qquad S_w\,(\Delta r) \qquad}^{} + \overbrace{\qquad S_{wd}\,(\Delta r)\,,}^{}$$

where $r' \equiv r + \Delta r$. Figure 7 shows the different components of the root phase structure function at different times during the simulation. The main points to note are that the shape of the structure function on small scales is similar for all components, with a power law slope close to $5/6$. The structure function turns over between $300 - 800$ m with the position of the turn over increasing with time. This growth in the turn over position is connected to the increase in height of the temperature inversion over this time period.

The relative amplitude of the different components changes as the simulation progresses, with the amplitude of the wet structure function decreasing relative to the dry structure function. This is likely to be because the atmosphere becomes better mixed as the simulation progresses, and this tends to reduce the amplitude of fluctuations. Meanwhile fluctuations in temperature and water vapour are created near the surface from the surface heat fluxes. Since the dry (sensible) heat flux is much larger than the latent heat flux, this tends to increase the fluctuations in the dry component faster than in the wet component. After two hours of convective activity, the r.m.s. wet phase fluctuations are 200 μm, while the r.m.s. dry phase fluctuations are 80 μm. The cross-correlation term ($S_{wd}\,(\Delta r)$) is positive at the start of the simulation, but as the simulation progresses, some scales become anti-correlated, and an oscillatory pattern is observed (at 0.75 hours). By the end of the two hours, the wet and dry phase fluctuations are anti-correlated on all scales. This transition to anti-correlated fluctuations can be understood by looking at the profiles of r.m.s. temperature and moisture fluctuations and the cross-correlation of water vapour with temperature with height in Fig. 6. Early on in the simulation, the dominant source of phase fluctuations is at lower levels (at heights in the range $200 - 400$ m), where the temperature and moisture fluctuations are positively correlated. As the simulation evolves the dominant source of phase fluctuations also moves upwards, and into the region where temperature and moisture are anti-correlated (above ~ 500 m, see Fig. 6), and so after two hours, the dominant source of the phase fluctuations comes from the region where temperature and moisture fluctuations are anti-correlated.

4.4.4 Phase variation with elevation

Figure 8 shows how the r.m.s. path changes with zenith angle (Z) for the dry, wet and total components of phase. The results are an average over ten simulations, and are normalised by the r.m.s. path at the zenith. The r.m.s. dry fluctuations are found to vary inversely with the cosine of the zenith angle (or linearly with air mass), while the r.m.s. wet fluctuations vary as the 0.75 power of air mass ($1/\cos^{0.75}[\mathrm{Z}]$). The combined total phase fluctuations vary as the square root of air mass, which is the dependence usually quoted for the variation of r.m.s. phase

with zenith angle (*e.g.* Evans *et al.*, 2003), and assumes an atmosphere with only short-range coherence in the refractive index fluctuations, and many independent fluctuations along the line of sight.

The steeper dependence of the dry and wet refractive index fluctuations can be explained by considering the location and shape of the main contributions to the temperature and moisture variance. The most significant refractive index fluctuations are located at the inversion, and these are created by convective plumes (transporting high moisture and low air temperature) which crash into the energy barrier posed by the inversion. As the plume hits the inversion its contents are spread out horizontally, and so these temperature and moisture fluctuations tend to be elongated horizontally, with only one or two different coherence patches in the vertical. The elevation dependence is therefore a function of the distance passed through the inversion layer, and this varies linearly with the air mass.

The shallower dependence of the total phase fluctuations on air mass is due to significant positive and negative correlations between the temperature and moisture fields that act to decrease the impact of the inversion (since the temperature and moisture field are anti-correlated here), and increase the impact of the convective plumes, where the temperature and moisture fields are positively correlated (this is shown in Fig. 9). As the zenith angle increases, the distance traversed within each plume decreases, but the number of plumes traversed increases.

4.4.5 Dry and wet phase correlation

Finally in this section we have measured the correlation coefficient between the dry phase and the wet phase (χ_{DW}), and the wet and dry phases with the total phase (χ_{WT}, χ_{DT}), for a line of sight at the zenith. The correlation coefficients are defined as:

$$\chi_{DW} \equiv \frac{\langle \phi'_w \phi'_d \rangle}{\langle {\phi'_w}^2 \rangle^{1/2} \langle {\phi'_d}^2 \rangle^{1/2}}; \qquad \chi_{WT} \equiv \frac{\langle \phi'_w \phi'_t \rangle}{\langle {\phi'_w}^2 \rangle^{1/2} \langle {\phi'_t}^2 \rangle^{1/2}}; \qquad \chi_{DT} \equiv \frac{\langle \phi'_d \phi'_t \rangle}{\langle {\phi'_d}^2 \rangle^{1/2} \langle {\phi'_t}^2 \rangle^{1/2}}. \quad (11)$$

The correlation coefficients and r.m.s. phases for the different components are summarised in Table 2, and show that there is a significant difference in behaviour between simulations that have no surface latent heat flux from the surface and those that do. As might be expected, the simulation with no latent heat flux has a much lower r.m.s. wet phase than the simulation with a source of water vapour from the ground by a factor of about two. Also, if there is no latent heat flux at the ground then there is significant anti-correlation between the wet and dry phases ($\chi_{DW} \simeq -0.7$), but the correlation between the total phase and the wet phase is about $\chi_{WT} \simeq 0.4$. If however there is a surface latent heat flux, then there is a high correlation between the wet and total phases ($\chi_{WT} \simeq 0.9$), and a lower anti-correlation between the wet and dry phases ($\chi_{DW} \simeq -0.2$). The difference in behaviour is due to there being significant positive correlation between the dry and wet fluctuations in the convective plumes if there is a surface latent heat flux, whereas there is a much lower correlation if there is no latent heat flux. These results suggest that water vapour radiometry is likely to track the total phase fluctuations to a high degree of accuracy if there is a source of water vapour from the ground.

Simulation	Hour	χ_{WT}	χ_{DT}	χ_{DW}	σ_T μm	$\sigma_D/\ \mu$m	$\sigma_W/\ \mu$m
A	2.0	0.4	0.6	-0.4	47	48	40
A	2.5	0.4	0.5	-0.6	48	54	51
A	3.0	0.3	0.5	-0.7	50	65	59
A	3.5	0.4	0.5	-0.6	58	66	63
A	4.0	0.5	0.2	-0.8	57	78	88
A	4.5	0.6	0.0	-0.8	64	91	113
B	2.0	0.9	0.4	-0.1	87	42	80
B	2.5	0.9	0.3	-0.2	102	44	100
B	3.0	0.9	0.2	-0.2	113	46	113
B	3.5	0.9	0.2	-0.2	125	50	126

Table 2: Table showing the cross correlation between the dry, wet and total phase components for simulations with two different surface latent heat flux values (simulation A has zero latent heat flux, and simulation B has 25 Wm^{-2}), and at different times through the simulation. χ_{WT} is the correlation coefficient between the wet phase and total phase components; χ_{DT} is between dry and total; and χ_{DW} is between wet and dry. σ_T, σ_D, and σ_W are the r.m.s. path lengths at zenith for the total, dry and wet components of the refractive index.

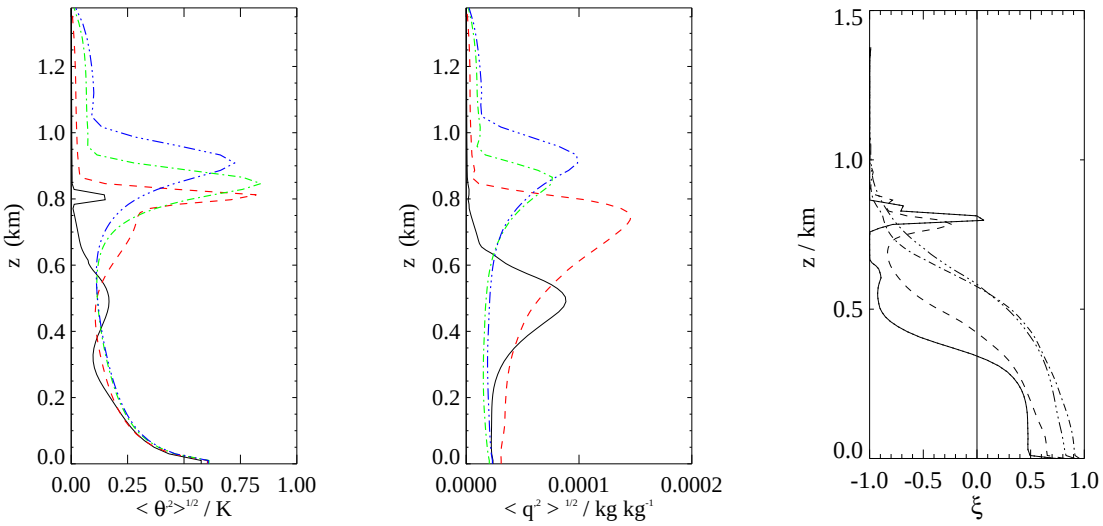

Figure 6: Left panel shows the root mean square spatial fluctuations in potential temperature. Centre panel shows the root mean square water vapour fluctuations. Right panel shows the cross-correlation between temperature and water vapour fluctuations. Profiles show the fluctuations from simulation B at 0.25 hours (solid lines), 0.75 hours (dashed), 1.5 hours (dot-dashed), and 2 hours (dot-dot-dot-dashed).

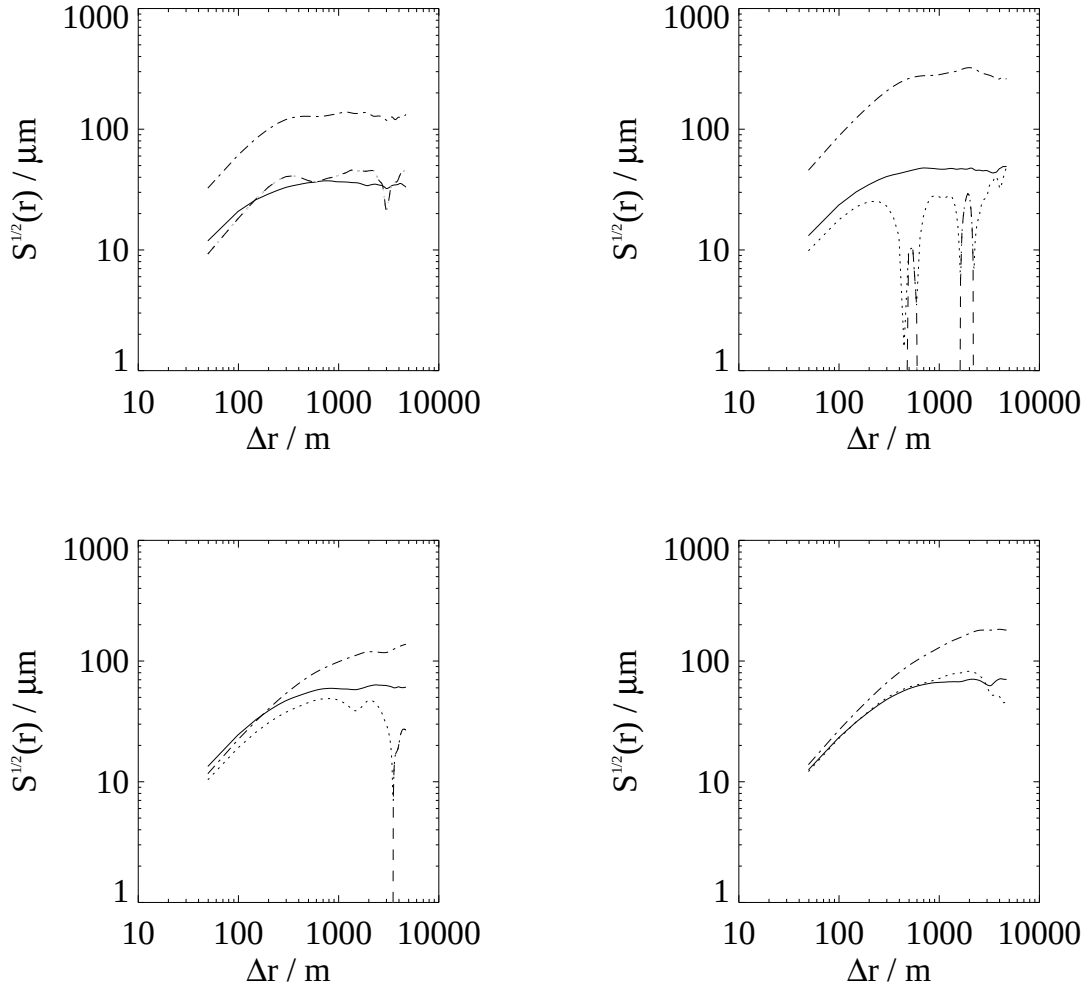

Figure 7: The different contributions to the root structure function, as defined in equation 10, and calculated from simulation B. Solid lines are for the dry contribution (*i.e.* $S_d^{1/2}$) , dot-dashed lines are for the wet contribution ($S_w^{1/2}$). The cross-correlation term ($S_{wd}^{1/2}$) uses dotted lines to show where there is anti-correlation ($S_{wd} < 0$), and dashed lines where there is a positive correlation, ($S_{wd} > 0$). Different panels show how the structure function changes after 0.25 hours (top left), 0.75 hours (top right), 1.5 hours (bottom left) and 2 hours (bottom right) of simulation.

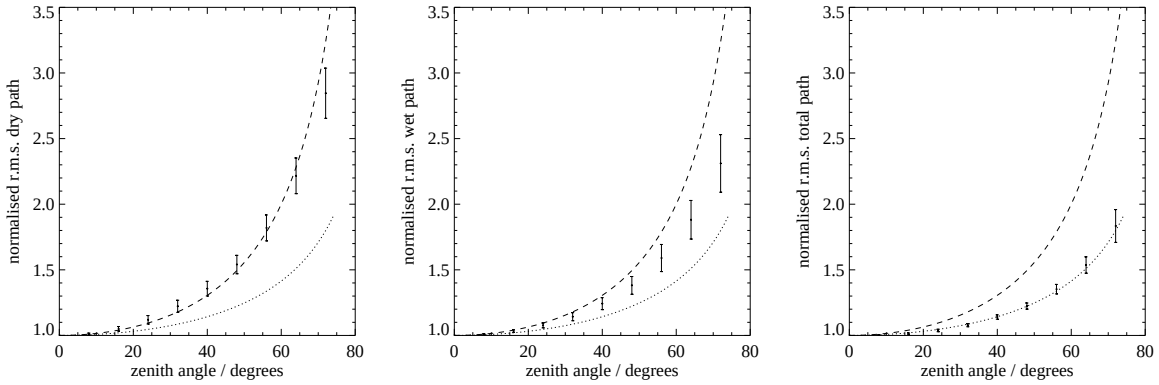

Figure 8: The variation in r.m.s. path with zenith angle for dry fluctuations (left), wet fluctuations (centre), and total wet and dry fluctuations combined (right). Results are calculated using both simulations A and B from two hours onwards. Dashed line shows how the air mass changes with elevation ($\propto 1/\cos[\mathrm{Zenith\ angle}]$), and dotted line shows the square root of the air mass ($\propto 1/\cos^{1/2}[\mathrm{Zenith\ angle}]$).

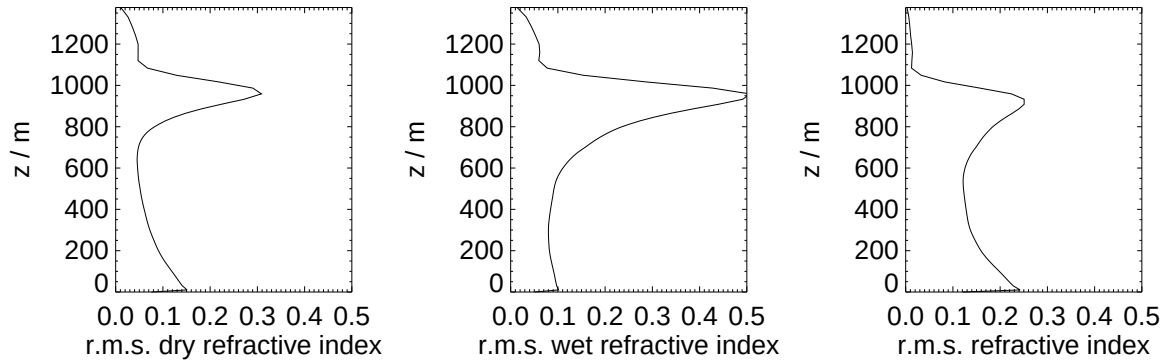

Figure 9: Vertical profiles showing the r.m.s. refractive index fluctuations from the dry (left), wet (centre), and total (right) contributions (taken from simulation B). While the inversion is dominant for both wet and dry components, the convective plumes become the dominant source when the wet and dry components are added together.

5 Scaling of the convective boundary layer

The convective boundary layer has been the subject of extensive study in meteorology, and a number of simple scaling laws have been found to apply universally to the case of an idealised convective boundary layer which is heated from the surface, and capped by a temperature inversion. We shall concentrate here on calculating the variances of temperature and moisture as they vary with height, which, from equation 5, can be related to the phase fluctuations.

5.1 Temperature variance

Sorbjan (1990) showed that beneath the temperature inversion, the temperature variance can be described as the sum of two terms – one that is controlled by the potential temperature flux at the ground ($\overline{w'\theta'}_0$), (where w' is the vertical velocity fluctuation, θ' is the potential temperature deviation from the mean, and the over-bar denotes the domain average at a given height – in this case at the ground) and another that is controlled by the potential temperature flux at the inversion ($\overline{w'\theta'}_i$). Sorbjan found that with a knowledge of these two fluxes, the potential temperature variance could be described as the following function of height, z:

$$\frac{\left\langle \theta'\left(z\right)^2\right\rangle}{{\theta_*}^2} = C_b\frac{\left(1-z/z_i\right)^{4/3}}{\left(z/z_i\right)^{2/3}} + C_t\mathcal{R}^{4/3}\frac{\left(z/z_i\right)^{4/3}}{\left(1-z/z_i+D\right)^{2/3}} \tag{12}$$

where z_i is the height of the temperature inversion, $\mathcal{R}$ is the ratio of the potential temperature flux at the inversion to the potential temperature flux at the surface, *i.e.* $\mathcal{R} = |\overline{w'\theta'}_i/\overline{w'\theta'}_0|$, $\theta_\star = \overline{w'\theta'}_0/w_\star$, where

$$w_\star = \left[\left(g/\theta_{v0}\right)z_i\overline{w'\theta'_v}_0\right]^{1/3}, \tag{13}$$

and $\theta_v = \theta\left(1+0.6q\right) \simeq \theta$ for the dry conditions at Chajnantor. C_b, C_t, D are constants that are found to be well approximated by: $C_b = \sqrt{2.25}$, $C_t = 6$, $D = 0$. This approximation works well for z in the range $0 < z < 0.9z_i$, however it diverges when $z/z_i = 1 + D$, and so the amplitude of the fluctuations across the inversion needs to be evaluated separately.

As the convective plume reaches the temperature inversion, the temperature variance is controlled by local quantities – namely the temperature gradient at the inversion, the speed at which the plume hits the inversion, and the strength of the energy barrier posed by the inversion (which is also a function of the vertical temperature gradient):

$$\left\langle \theta'\left(z\right)^2\right\rangle = C\frac{\overline{w\left(z\right)^2}}{N^2}\left(\frac{\partial\theta}{\partial z}\right)^2, \tag{14}$$

where $C \simeq 3.2$, $N^2 = \left(g/\theta_0\right)d\theta/dz$, and $\overline{w^2}$ is the vertical velocity variance.

5.2 Water vapour variance

We can write down similar expressions for the variance of water vapour:

$$\frac{\left\langle q'\left(z\right)^2\right\rangle}{{q_\star}^2} = C_b\frac{\left(1-z/z_i\right)^{4/3}}{\left(z/z_i\right)^{2/3}} + C_t{\mathcal{R}_Q}^2\mathcal{R}^{-2/3}\frac{\left(z/z_i\right)^{4/3}}{\left(1-z/z_i+D\right)^{2/3}}. \tag{15}$$

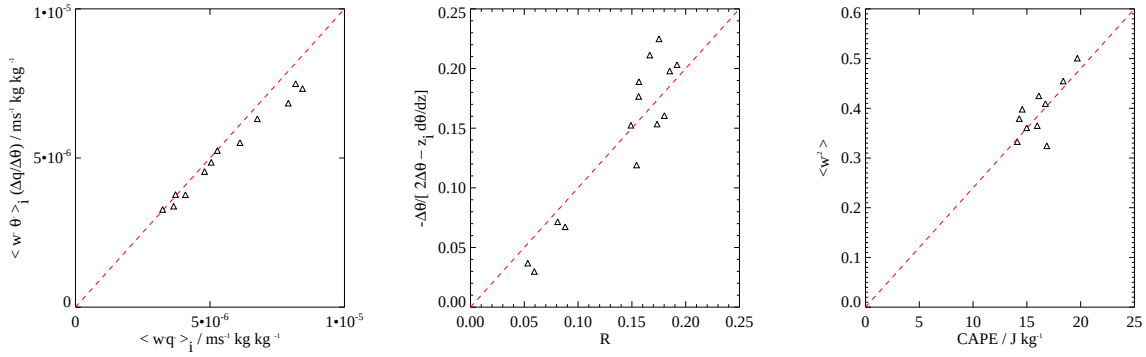

Figure 10: Tests of the scalings outlined in subsections 5.3, 5.4, and 5.5. In each case the dashed line represents the theoretical relation. Left panel: A scaling for $\overline{w'q'}$ at the inversion as a function of $\overline{w'\theta'}$ (see equation 18). Centre panel: a scaling for $\mathcal{R}$ using equation 20. Right panel: scaling for $\overline{w^2}$ as a function of CAPE, dashed line is a fitted straight line: $\overline{w^2} = 0.024(\mathrm{CAPE})$. (Data from the second hour onwards from both simulations, A and B, are shown).

Here $\mathcal{R}_Q$ is the ratio of the water vapour flux at the inversion to that at the surface, *i.e.* $\mathcal{R}_Q = \overline{w'q'}_i/\overline{w'q'}_0$, and $q_\star = \overline{w'q'}_0/w_\star$.

At the inversion, *i.e.* $z > 0.9z_i$, the variance can be linked to its local gradient, as with the temperature variance:

$$\langle q'(z)^2 \rangle = C\frac{\overline{w(z)^2}}{N^2}\left(\frac{\partial q}{\partial z}\right)^2. \tag{16}$$

The interest of these relations is the possibility of relating the variances of potential temperature and water vapour to the mean vertical profiles of temperature and water vapour. From this we can deduce the strength of fluctuations from radiosonde profiles, which can then be related to phase fluctuations. In the next three subsections we concentrate on removing terms that depend on quantities that are not measured by the radiosonde profiles. These are the fluxes at the top of the temperature inversion (found in $\mathcal{R}$, and $\mathcal{R}_Q$), and the vertical velocity variance, $\overline{w^2}$.

5.3 Relating $\mathcal{R}$ and $\mathcal{R}_Q$

We start by showing how the temperature and water vapour fluxes at the inversion can be related to each other. Following Garratt (1992; p153), in the convective boundary layer, the flux of a conserved quantity, c (such as θ and q) at the top of the boundary layer is given by:

$$(\overline{w'c'})_i = \Delta c[\partial z_i/\partial t - w_h], \tag{17}$$

where z_i is the height of the inversion, w_h is a vertical advection term, and $\Delta c = c_i - c_m$ with the subscripts m and i denoting values in the mixed layer and at the inversion respectively. Since the term $[\partial z_i/\partial t - w_h]$ is the same for all conserved quantities, we can use this to find a relation between the potential temperature flux, and the water vapour flux:

$$(\overline{w'q'})_i = \frac{\Delta q}{\Delta\theta}(\overline{w'\theta'})_i. \tag{18}$$

Since in general we can measure the flux at the surface, this allows us to find a relationship between $\mathcal{R}$ and $\mathcal{R}_Q$:

$$\mathcal{R}_Q = \frac{(\overline{w'\theta'})_0}{(\overline{w'q'})_0}\frac{\Delta q}{\Delta\theta}\mathcal{R}. \tag{19}$$

The left hand panel of Fig. 10 is a plot of the left and right hand sides of equation 18 taken from the simulations described in section 4. It shows that this approximation holds to within around 5% for the simulations used here.

5.4 Relation of $\mathcal{R}$ to mean quantities

Now that we have related the water vapour flux to the temperature flux at the inversion, if we can find an expression for the temperature flux, then we can obtain both $\mathcal{R}$, and $\mathcal{R}_Q$. Again, following Garratt (1992; p155), an expression for the ratio of the flux at the top of the boundary layer to the flux at the surface can be obtained:

$$\mathcal{R} = \frac{-\Delta\theta}{2\Delta\theta - z_i(d\theta/dz)_i}, \tag{20}$$

where $\Delta\theta$ is the change in θ across the inversion. In outline this relation comes from solving a homogeneous differential equation that was constructed using the conservation relation for a conserved variable:

$$\frac{\partial c}{\partial t} = -\frac{\partial(\overline{w'c'})}{\partial z} \tag{21}$$

and equation 17 (see also *e.g.* Betts, 1973, 1974). The performance of this approximation is shown in the centre panel of Fig. 10 and shows that it fits the simulation data to within about 10%.

5.5 Velocity variance

In order to be able to relate our equations of potential temperature and water vapour variance to radiosonde profiles, we need to find an expression for the velocity variance, $\overline{w^2}$ in equations 14 and 16. The velocity variance near the inversion can be linked to the convective available potential energy, CAPE (see Appendix, Subsection 10.4 for definition). Since there is dissipation at the edges of the updraughts, and a certain amount of energy is converted into kinetic energy of the compensating descent, we can parametrise the velocity variance near the inversion to be:

$$\overline{w^2}\,(z_i) = \delta\mathrm{CAPE}, \tag{22}$$

where δ is a constant that can be measured from numerical simulations. The vertical velocity variance decays exponentially above this point, and so we can parametrise the velocity variance above the inversion to be:

$$\overline{w^2}\,(z) = (\delta\mathrm{CAPE})\exp[-(z - z_i)/z_d], \tag{23}$$

where z_d can also be found from the simulations.

The right hand panel of Fig. 10 shows how the velocity variance depends on CAPE. This appears to have a linear relationship to within around 10%, with the parameter δ estimated to be: $\delta = 0.024$. z_d was found to be well fit by $z_d = z_i/6$.

Finally we substitute the approximations in Subsections 5.3, 5.4 and 5.5 into the approximations for the variances in Subsections 5.1, and 5.2. This allows us to estimate the variance of temperature and water vapour from their mean profiles alone (as could be deduced from a radiosonde profile). Here we use the variance equations 12, 14, 15, and 16, combined with equations 19, 20, 22 and 23 for the second order terms. A comparison between the approximations for the variance and the measured variance is shown in Fig. 11. It shows that there is good agreement, with a maximum difference in the fit of less than 15%.

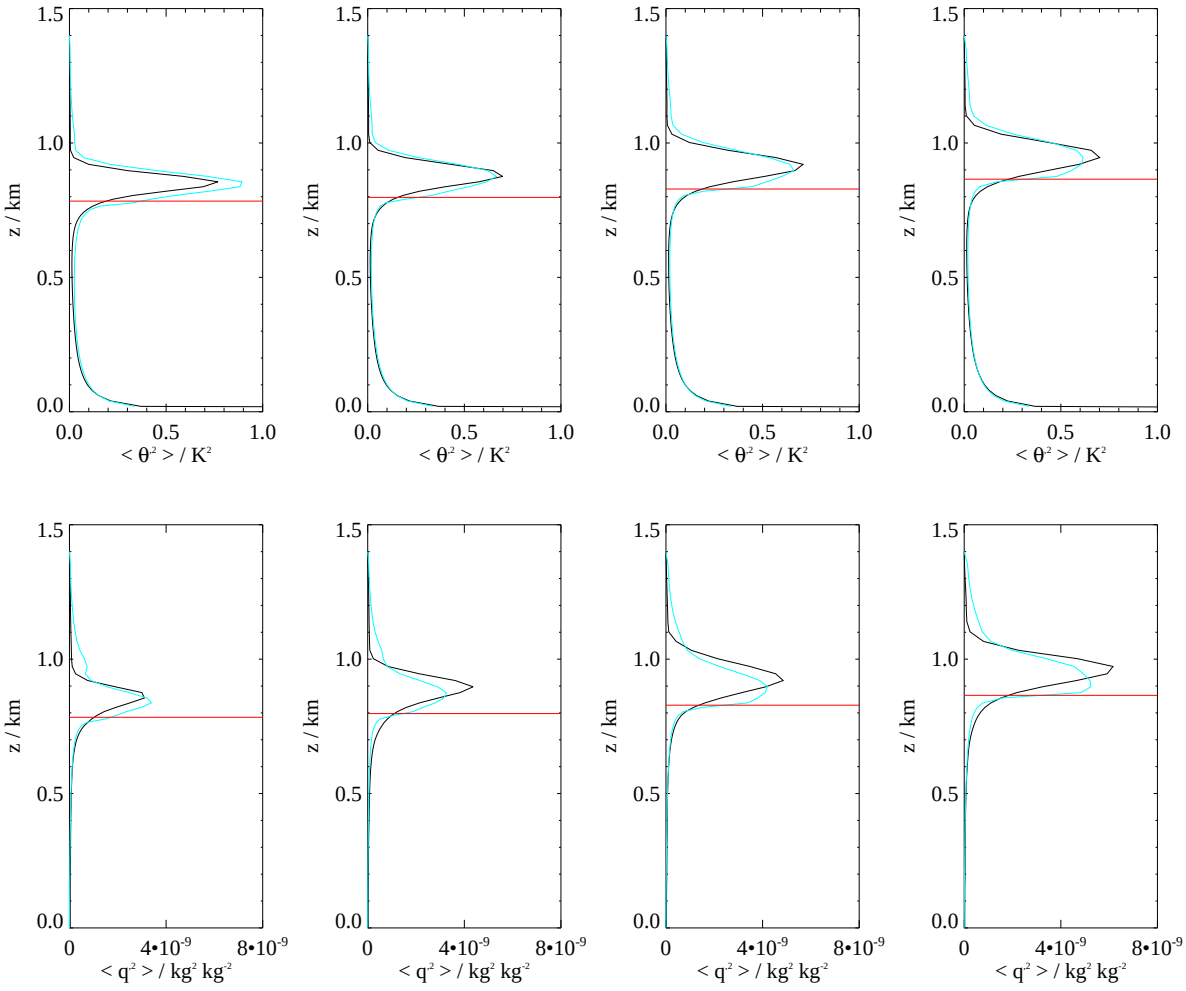

Figure 11: Mean square fluctuations (dark lines) in potential temperature (top panels), and water vapour (bottom panels), with Sorbjan's predictions (equations 12–16) combined with parametrisations for $\mathcal{R}$, $\mathcal{R}_Q$ and $\overline{w^2}$ from equations 19, 20, and 22 overlaid (lighter lines). The horizontal line shows the location of the base of the inversion. From left to right, the left-most panels are after 2 hours of simulation, second panels after 2.5 hours, third panels after 3 hours, and fourth panels (right-most) after 3.5 hours. Profiles plotted are for simulation A, (similar fits are achieved for simulation B).

6 Linking variance relations to path fluctuations

The final stage is to relate the fluctuations in temperature and water vapour to path length fluctuations. The path length is given in equation 9, and the variance of path length is given by:

$$\langle \mathcal{L}^2 \rangle - \langle \mathcal{L} \rangle^2 = \iint \langle n'(y_1)\, n'(y_2) \rangle dy_1 dy_2 \tag{24}$$

$$= \iint A^2 \langle \theta'(y_1)\, \theta'(y_2) \rangle + B^2 \langle q'(y_1)\, q'(y_2) \rangle + 2AB \langle \theta'(y_1)\, q'(y_2) \rangle dy_1 dy_2, \tag{25}$$

where $A = \alpha R \overline{\rho}_T / (\mathcal{M}_d \overline{\theta})$, and $B = \gamma R \overline{\rho}_T / (\mathcal{M}_v \overline{T})$, as in equation 5. In order to evaluate these integrals, we need to find an approximation for the correlations between the temperature and moisture fluctuations at different heights. Here we adopt a somewhat empirical approach, using information from the simulations to estimate a possible form and amplitude for the cross- and auto-correlation terms in equation 25. One way of describing the correlations at different heights through the simulation is to consider that fluctuations are correlated over a certain length scale, ζ, with the correlation between different patches falling off as a Gaussian profile. This would allow us to rewrite the auto-correlation terms in equation 25 as

$$\langle \theta'(y_1)\, \theta'(y_2) \rangle \simeq \langle \theta'(y_1)^2 \rangle^{1/2} \langle \theta'(y_2)^2 \rangle^{1/2} \exp[(y_1 - y_2)^2 / 2\zeta^2] \tag{26}$$

$$\langle q'(y_1)\, q'(y_2) \rangle \simeq \langle q'(y_1)^2 \rangle^{1/2} \langle q'(y_2)^2 \rangle^{1/2} \exp[(y_1 - y_2)^2 / 2\zeta^2]. \tag{27}$$

This approximation is found to work well for $\zeta = z_i/12$ and when y_1 and y_2 are either both less than the height of the inversion, or both greater than the height of the inversion, however, when y_1 and y_2 lie on either side of the inversion, this approximation breaks down. This is because it neglects the existence of longer range correlations that arise because of the motion of the plumes – positively buoyant plumes at the surface rise until they crash into the energy barrier created by the temperature inversion and become negatively buoyant. This produces negative correlations in the temperature field across the inversion. Conversely, the moisture field is subject to long-range positive correlations across the inversion along the direction of motion of the plume. This is because the moisture profile tends to decrease with height, falling off sharply at the inversion, and so a rising plume tends to be moister than the environment at all heights, and therefore gives rise to positive correlations.

If we call values along the line of sight that are above the inversion y^+, and values along the line of sight that are below the inversion y^-, then we can write:

$$\langle \theta'\left(y_1^+\right) \theta'\left(y_2^-\right) \rangle \simeq \chi_{\theta^+\theta^-} \langle \theta'(y_1)^2 \rangle^{1/2} \langle \theta'(y_2)^2 \rangle^{1/2} \tag{28}$$

$$\langle q'\left(y_1^+\right) q'\left(y_2^-\right) \rangle \simeq \chi_{q^+q^-} \langle q'(y_1)^2 \rangle^{1/2} \langle q'(y_2)^2 \rangle^{1/2} \tag{29}$$

where we make the simplifying approximation that χ is a constant that can be measured from the simulation. For the above relations we find $\chi_{\theta^+\theta^-} \sim -0.25$, and $\chi_{q^+q^-} \sim 0$ when there is no latent heat flux from the ground, and $\chi_{q^+q^-} \sim 0.35$ when there is a source of latent heat flux from the ground. The different behaviour depending on the presence of a surface latent heat flux is to be expected, since in the absence of a source of moisture from the ground, the water vapour profile tends towards a constant value, and so the convective plumes do not contain more water vapour than the environment. There is therefore little correlation between the moisture content beneath the inversion and the other variables. If, however, there is a source of water

Simulation	$\overline{w'q'}_0$	$\chi_{\theta^+\theta^-}$	$\chi_{q^+q^-}$	$\chi_{\theta^+q^+}$	$\chi_{\theta^-q^-}$	$\chi_{\theta^+q^-}$	$\chi_{\theta^-q^+}$	ζ
A	0	-0.25	0	-0.6	0	0	0.1	$z_i/12$
B	$25\,\mathrm{Wm}^{-2}$		0.35	-0.35	0.1			

Table 3: Table showing the correlation coefficients between variables θ^+, θ^-, q^+, and q^- where θ is potential temperature, q water vapour, and $+$ indicates a level above the inversion, and $-$ indicates a level below the inversion. In some cases, a different value is required when there are moisture fluxes from the ground. If only one value is quoted, this is applicable to both zero and non-zero latent heat flux scenarios. Values have been estimated combining results between the second and fourth hours of the simulations.

vapour from the ground, then the plumes carry moisture upwards from the ground, and so tend to be wetter than the environment. In this case, correlations between the water vapour above the inversion and that below are expected, as well as with the temperature fluctuations above and below the inversion.

We can treat the cross-correlation term similarly *i.e.* :

$$\langle \theta'(y_1)\, q'(y_2) \rangle = \chi_{\theta q} \langle \theta'(y_1)^2 \rangle^{1/2} \langle q'(y_2)^2 \rangle^{1/2} \tag{30}$$

where $\chi_{\theta q}$ takes four different values depending on whether y_1 and y_2 are both below the inversion, both above the inversion, or on either side of the inversion. Table 3 gives a summary of the correlation coefficients measured from the simulations.

Substituting equations 26-30 into equation 25, and using the correlation coefficients shown in Table 3, equation 25 can be integrated to obtain an estimate for the variance in path length due to variations in potential temperature and water vapour. Furthermore if we use Sorbjan's estimates for the temperature and water vapour variances (equations 12–16), this estimate for the variance in path length can be derived only using information relating to the mean profiles of temperature and water vapour, and can therefore be used to derive estimates for the variance in path length from radiosonde profiles. Figure 12 shows how the estimate for the r.m.s. path fluctuations due to dry and wet refractive index fluctuations compares with the values measured directly from the simulations, and shows that there is an agreement between the estimator and the true values to within about 10%. We are now in a position to apply the same method to obtain an estimate for the dry and wet fluctuations present at Chajnantor during convective conditions, using radiosonde data taken from the site.

7 Application to radiosonde profiles

Finally we have used data from 35 radiosonde profiles launched between 15 UT and 21 UT (corresponding to between midday and 1800 local time) to estimate the likely r.m.s. dry and wet path length fluctuations. (For a list of the ascents used, see Table 5 in the appendix). Figure 13 shows an example set of profiles taken from a radiosonde ascent (1998-11/98112720.dat). The left two panels show the water vapour and potential temperature profiles, showing that the water vapour and potential temperature are near constant at heights up to 1000 m above ground level. The lines on the potential temperature plot illustrate the position of the top of the mixed layer (z_i), which has been calculated as the point at which the vertical gradient in potential

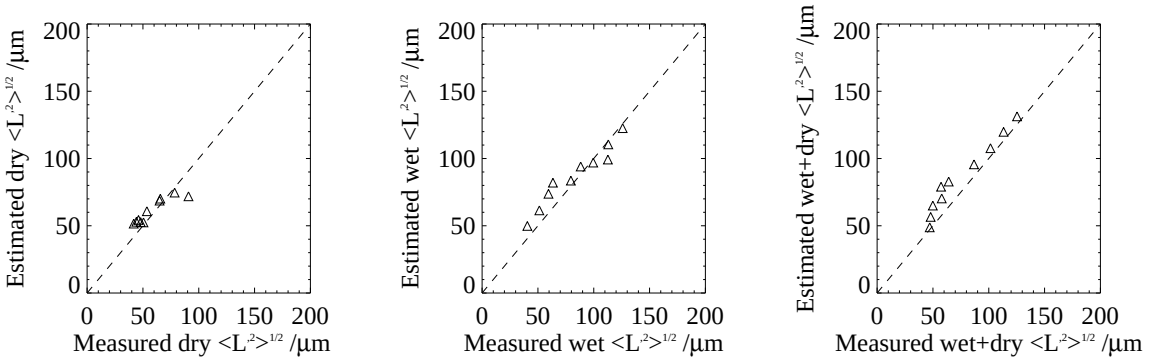

Figure 12: Estimation of the r.m.s. path length fluctuations for the dry (left panels), wet (centre panels), and total (right panels) components calculated from hour 2 onwards in simulations A and B.

temperature exceeds 0.01 K m^{-1}; the top of the inversion layer (where the temperature gradient decreases to a small fraction of the inversion strength); and the values taken to represent the mixed layer potential temperature; the parcel temperature in the calculation of CAPE (see Appendix 10.4 for definition); and the potential temperature at the top of the inversion layer. We have identified these values for each of the radiosonde profiles used, and followed the same method as described in the previous sections to calculate the fluctuations in water vapour and potential temperature. The only additional requirements have been to calculate the surface heat and water vapour fluxes. For this we have used the following relation Garratt (3.32a):

$$\overline{w'\theta'}_0 = -\frac{d\theta}{dz} z^{4/3} \left(\frac{g}{\alpha \theta^{1/3}} \right)^{3/2}, \tag{31}$$

where α is a constant close to 0.7, and the water vapour flux can be obtained from:

$$\frac{\overline{w'\theta'}_0}{\overline{w'q'}_0} = \left(\frac{d\theta}{dz} \right) \left(\frac{dq}{dz} \right)^{-1}. \tag{32}$$

From these estimates, we find a mean heat flux value of 280 W m^{-2}, and a water vapour flux of around 50 W m^{-2}, both somewhat higher than the values used in the simulations in the previous section. The heights of the inversion layer were found to range between 725 and 1700 m.

The right two panels of Fig. 13 show the estimates for the potential temperature variance, and water vapour variance for the radiosonde profile shown. The resulting predictions for the r.m.s. path length for dry, wet and total contributions are shown in Fig. 14. The top left panel shows a scatter plot of the estimated dry and wet path length fluctuations for all the radiosonde ascents. It shows that more than half of the time the wet fluctuations exceed the dry fluctuations. The top right panel of Fig. 14 is a scatter plot of the wet fluctuations vs the total fluctuations. It shows that there is a very high correlation between these two values, suggesting that a measure of the r.m.s. wet fluctuations may give an indication of the r.m.s. total fluctuations. The bottom left panel of Fig. 14 shows the cumulative distribution of dry, wet and total path fluctuations, with the values quoted for the total r.m.s. path fluctuations in Evans *et al.* (2003)[2] overlaid. It

[2]The results quoted in Evans *et al.* (2003) are for the r.m.s. phase *difference* between two lines of sight separated by 300 m. In this work we have used the r.m.s. phase for a single line of sight, and so the Evans results have been divided by $\sqrt{2}$ for comparison.

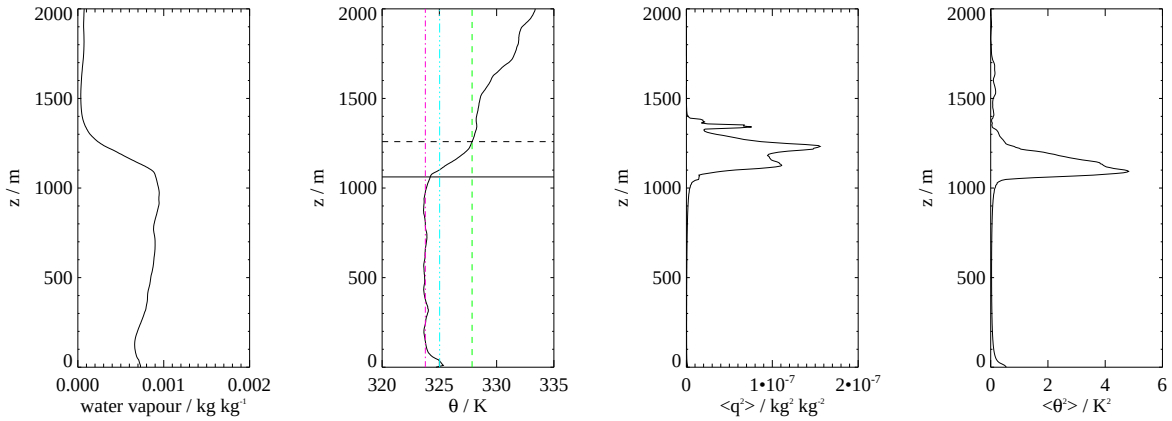

Figure 13: Example radiosonde profiles of water vapour (left), potential temperature (second from left), with associated estimates for the variance in water vapour (third from left), and variance in potential temperature (right). Lines on the potential temperature plot represent the top of the mixed layer (solid horizontal), the top of the inversion layer (dashed horizontal), the mean potential temperature in the mixed layer (dot-dashed vertical), the potential temperature at the ground (dot-dot-dot dashed vertical) and the potential temperature at the top of the inversion layer (dashed vertical).

shows that there is good agreement between the interferometer measurements and the results derived from the radiosonde measurements, and that the contribution from the dry fluctuations is about half of that from the water vapour fluctuations. At the 25% level the r.m.s. fluctuations are found to be 100 μm for the dry component, 180 μm for the wet component, and 240μm for the total r.m.s. path. At the 75% percentile these increase to 200, 530, and 525 μm for the dry, wet and total contributions respectively (see Table 4).

Finally we have estimated the level of correlation between the wet and total phase components (χ_{WT} as in equation 11). This is shown as a cumulative distribution in Fig. 14 (bottom right), and corresponds to values greater than 0.97, 0.92, and 0.75 for 25%, 50% and 75% of the time respectively, so that for 25% of the time, (during daytime convective conditions), the wet path fluctuations trace at least 97% of the total path fluctuations, and 75% of the time, the wet path fluctuations trace at least 75% of the total path fluctuations. This suggests that during some of the worst phase conditions at Chajnantor, water vapour radiometry is expected to be able to correct for a high fraction of the phase variations present.

	$\phi_{\rm rms}^{\rm dry}$ / μm	$\phi_{\rm rms}^{\rm wet}$ / μm	$\phi_{\rm rms}^{\rm total}$ / μm	χ_{WT}
75%	200	530	525	0.97
50%	140	335	345	0.92
25%	100	180	240	0.75

Table 4: The estimated percentiles for the dry, wet and total contributions to refractive index path fluctuations based on an analysis of radiosonde ascents between 17-21 UT.

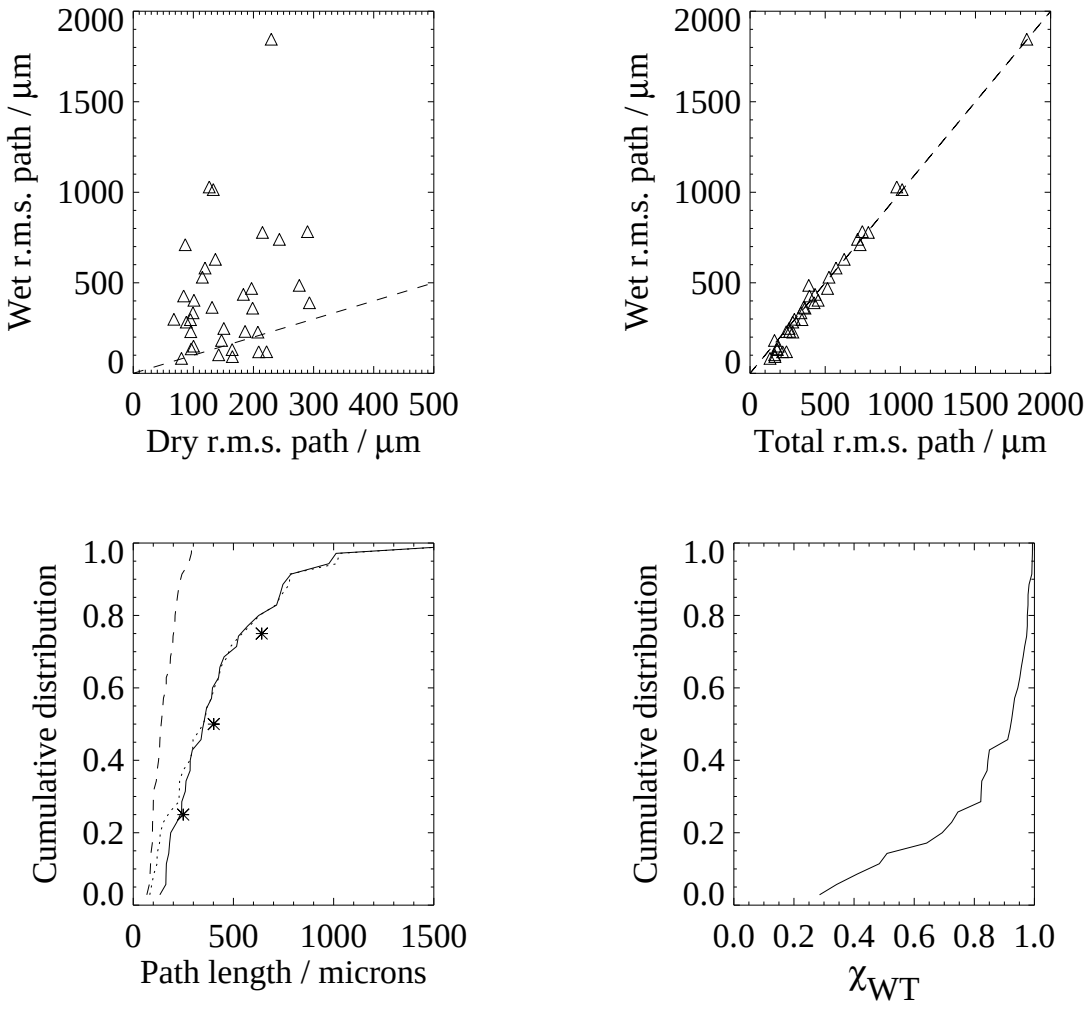

Figure 14: Top left: Scatter plot showing the estimated dry and wet fluctuations for each radiosonde profile used. Dashed line shows where the wet and dry fluctuations are equal. Top right: Scatter plot showing the estimated total and wet fluctuations for each radiosonde profile. Bottom left: cumulative distribution of dry fluctuations (dashed), wet fluctuations (dotted), and total fluctuations (solid). Stars show the interferometer measurements of the total r.m.s. fluctuations from Evans *et al.*, 2003 for comparison. Bottom right shows the cumulative distribution of correlation coefficients between the wet and total phase fluctuations.

8 Conclusions

In this report we have presented results from simulations of the daytime atmosphere at Chajnantor, during which convection is the main generator of refractive index fluctuations.

The main results from this report are summarised below:

- ◇ **Structure function.** We have used the simulations to measure the phase structure function expected during daytime conditions (Fig. 7). This is found to have a Kolmogorov turbulence spectrum (with power law $5/3$) on small scales, and turns over on a scale of order the height of the inversion layer.

- ◇ **Variation of r.m.s. phase with elevation.** Our simulations confirm that the total r.m.s. phase varies with the square root of the air mass, however the dry component is shown to vary linearly with air mass, while the wet component varies as the air mass to the power 0.75 (see Fig. 8).

- ◇ **Location of phase fluctuations.** The dry phase fluctuations were found to be concentrated near to the ground and at the temperature inversion, while the wet phase fluctuations were predominantly concentrated at the inversion. In contrast, however, the combined total phase contribution was found to be more evenly distributed within the layer, with significantly lower contribution from fluctuations at the inversion (Fig. 9). This difference in behaviour is due to significant anti-correlation between the water vapour and temperature fields at the inversion, along with a positive correlation between the two fields below the inversion.

- ◇ **Estimation of the dry and wet components of phase at Chajnantor.** We have used theoretical scaling arguments combined with numerical simulations to derive a relationship between the r.m.s. path fluctuations and the mean profiles of water vapour and potential temperature. This relation was applied to radiosonde profiles launched during the daytime at Chajnantor. Fig. 14 shows the range of expected r.m.s. dry, wet, and total phase fluctuations. At the $25^{\rm th}$ percentile the dry, wet and total components were found to be ~ 100, 180, 240 μm respectively. At the $50^{\rm th}$ percentile these increase to 140, 335, 345 μm, and at the $75^{\rm th}$ percentile the values are 200, 530, 525 μm. We have compared these estimates with independent measurements of the total r.m.s. phase obtained from interferometric measurements (Evans *et al.*, 2003), and these show excellent agreement.

- ◇ **Performance limits of water vapour radiometry during daytime convective conditions.** We have estimated the correlation between wet and total path fluctuations from the radiosonde profiles. These show a high positive correlation, with values greater than 0.97, 0.92, 0.75 corresponding to the 25, 50 and 75 percentiles respectively (Fig. 14). These values indicate that 75% of the time (during daytime convective conditions), the water vapour radiometers will be sensitive to over 75% of the total phase variations present, while for 25% of the time, it will be sensitive to over 97% of the total phase variations, and suggests that during some of the worst phase conditions present at Chajnantor (daytime early afternoon) water vapour radiometry will be able to remove a significant fraction of the phase variations.

9 References

Baumer, O.W. 1990 'Prediction of soil hydraulic parameters.' In: WEPP Data Files for Indiana. SCS National Soil Survey Laboratory, Lincoln, NE.

Betts, A. K. 1973 'Non-precipitating cumulus convection and its parametrization' *Quart. J. Roy. Met. Soc.* **99,** 178-96

Betts, A. K. 1974 'Reply to comment on the paper "Non-precipitating cumulus convection and its parametrization"' *Quart. J. Roy. Met. Soc.* **100,** 469-71

Evans, N., Richer, J. S., Sakamoto, S.,Wilson, C., Mardones, D., Radford, S., Cull, S., Lucas, R. 2003 'Site Properties and Stringency' *ALMA Memo* **471**

Garratt, J. R. 1992 'The atmospheric boundary layer' *Cambridge Atmospheric and Space Science Series*, CUP.

Gray, M. E. B. 2000 'Characteristics of numerically simulated mesoscale convective systems and their application to parameterization.' *J. Atmos. Sci.*, **57,** 3953-3970

Gray, M. E. B., Petch, J., Derbyshire, S. H., Brown, A. R., Lock, A. P., Swann, H. A., Brown, P. R. A. 2001 Version 2.3 of the Met Office large eddy model. Part II. Scientific documentation. Turbulence and Diffusion Note 276

Radford, S. 2000 `http://www.tuc.nrao.edu/mma/sites/Chajnantor/`

Sorbjan, Z. 1990 'Similarity Scales and Universal Profiles of Statistical Moments in the Convective Boundary Layer' *J. Applied Meteorology* **29** 762

10 Appendix

In this appendix we list a few basic definitions of terms and parameters that are used throughout this memo.

10.1 Potential temperature, θ

Potential temperature is the temperature that would result if a parcel of air were brought adiabatically to a reference pressure, p_0. It is derived from the ideal gas law and first law of thermodynamics, and is given by:

$$\theta = T\left(\frac{p}{p_0}\right)^{R_d/c_p}, \tag{33}$$

where T is the temperature in Kelvin, p is the pressure in Pa, and p_0 is generally taken to be 10^5 Pa. $R_d = 287.04$ J kg^{-1} K^{-1} is the gas constant for dry air, $c_p = 1004.5$ J kg^{-1} K^{-1} is the specific heat capacity of air at constant pressure. An important property of potential temperature in dry atmospheres (such as at Chajnantor) is that it is a conserved quantity *i.e.* in the absence of mechanical mixing, air parcels keep the same potential temperature under adiabatic, vertical motion.

10.2 Atmospheric stability

The stability of a dry atmosphere (such as at Chajnantor) is defined in terms of the vertical gradient of potential temperature. In a *stable atmosphere* the potential temperature increases with height, so an air parcel lifted from a lower level, will have a lower potential temperature than the surrounding environment, and will therefore be negatively buoyant. If the air parcel is released at this point, it sinks, and executes simple harmonic motion about its level of neutral buoyancy. The frequency of its oscillation is given by the Brunt-Väisälä frequency, N, where $N^2 = (g/\theta)d\theta/dz$. A *neutral atmosphere* has zero gradient in θ, and an *unstable atmosphere* has a negative gradient of θ, so that a parcel of air displaced upwards will be positively buoyant, and continue rising until is reaches a new position of neutral buoyancy.

10.3 Boundary layer

By this we refer to the lowest layer of the troposphere that is influenced by the surface heat fluxes. In the case of the daytime convective boundary layer, this is generally capped by a temperature inversion, so the boundary layer depth is equivalent to the height of the temperature inversion above the ground. The depth varies throughout the day, but during the peak of convective activity it can reach 1 km in extent.

10.4 Convective Available Potential Energy (CAPE)

The stability of the atmosphere can be used to determine whether the atmosphere will support convective motion, and a measure of the amount of gravitational potential energy stored in the atmosphere can give an indication of the likely strength of convective activity. The convective available potential energy (or CAPE) is a measure of the gravitational potential energy stored in the atmosphere, and is defined as:

$$\mathrm{CAPE} = g \int_{z_0}^{z_i} \frac{\theta_p - \theta_e}{\theta_e} dz, \tag{34}$$

where θ_p is the potential temperature of an air parcel coming from level z_0. θ_e is the potential temperature of the environment at level z. z_i is the top of the convective layer, and in the boundary layer this is generally the height of the temperature inversion. During convection, CAPE is converted into kinetic energy, and in the absence of any mixing of the updraught air with the environment, the kinetic energy of the updraughts (per unit mass) would be given directly by the CAPE. In practice, however, the mixing of updraught air with the surroundings removes some of the available potential energy, and so only a fraction of the CAPE is converted into kinetic energy, with the rest being dissipated as heat.

Year-month	UT	R'sonde number	Wet r.m.s. / μm	Dry r.m.s. / μm	Total r.m.s / μm	χ_{WT}
1998-10	18	98100917	164.9	92.4	165.4	0.29
1998-10	18	98101218	96.4	135.1	177.1	0.84
1998-11	21	98112521	133.1	1015.0	1012.3	0.99
1998-11	16	98112615	136.6	629.7	626.3	0.98
1998-11	21	98112621	67.6	298.6	294.9	0.97
1998-11	20	98112720	99.4	334.2	338.3	0.96
1998-12	16	98120515	88.3	282.9	283.8	0.95
1998-12	15	98120915	207.3	227.8	284.5	0.69
1998-12	15	98121115	276.3	486.0	390.6	0.82
1999-03	16	99030915	86.5	710.4	732.0	0.99
1999-11	20	99110319	95.1	296.6	345.3	0.97
1999-11	19	99110518	119.4	581.7	571.9	0.98
1999-11	19	99110618	83.9	427.5	395.5	0.98
1999-11	19	99110718	221.9	119.3	242.3	0.41
1999-11	20	99110719	229.6	1845.5	1841.2	0.99
1999-11	19	99110819	164.6	131.1	181.4	0.48
1999-11	19	99110918	215.0	778.3	787.1	0.96
1999-11	19	99111018	243.1	740.2	715.1	0.94
2000-06	19	00062618	208.7	118.8	217.0	0.34
2000-07	19	00071219	80.2	82.6	132.8	0.82
2000-07	20	00071319	142.1	102.6	163.6	0.51
2000-07	19	00072818	293.1	390.0	425.9	0.75
2000-07	18	00073118	101.0	403.8	453.3	0.98
2000-12	19	00121318	150.7	248.0	259.7	0.82
2000-12	19	00121418	183.2	436.3	432.3	0.91
2000-12	19	00121518	186.0	231.5	263.4	0.72
2000-12	19	00121618	126.4	1029.4	976.0	0.99
2001-04	20	01042619	100.3	150.2	187.1	0.85
2001-04	19	01042819	115.0	531.0	525.1	0.98
2001-05	19	01050119	196.8	468.9	515.7	0.92
2001-12	19	01120719	198.5	359.9	365.3	0.85
2001-12	20	01120919	289.9	782.8	747.0	0.93
2001-12	20	01121019	146.8	181.9	162.5	0.64
2001-12	20	01121119	95.6	230.0	241.2	0.92
2001-12	20	01121219	131.1	364.4	356.1	0.93

Table 5: Table listing the radiosonde ascent profiles used in this work, with estimations of the wet, dry and total r.m.s. phase, and the correlation coefficient between wet and total fluctuations.